Superlattices and Microstructures 113 (2018) 483–496

Contents lists available at ScienceDirect

Superlattices and Microstructures

journal homepage: www.elsevier.com/locate/superlattices

Asymmetrical external effects on transmission, conductance and giant tunneling magnetoresistance in silicene

O. Oubram [a, *], O. Navarro [b], E.J. Guzmán [b, c], I. Rodríguez-Vargas [d]

[a] Facultad de Ciencias Químicas e Ingeniería, Universidad Autónoma Del Estado de Morelos, Av.Universidad 1001, Col. Chamilpa, 62209, Cuernavaca, Morelos, Mexico
[b] Unidad Morelia del Instituto de Investigaciones en Materiales, Universidad Nacional Autónoma de México, Antigua Carretera a Pátzcuaro No. 8701, Col. Ex Hacienda de San José de La Huerta, 58190, Morelia, Michoacán, Mexico
[c] Facultad de Ciencias Físico Matemáticas, Universidad Michoacana de San Nicolás de Hidalgo, Av. Francisco J. Mujica S/n Ciudad Universitaria, Morelia, Michoacán, Mexico
[d] Unidad Académica de Física, Universidad Autónoma de Zacatecas, Calzada Solidaridad Esquina con Paseo La Bufa S/N, 98060, Zacatecas, Zac., Mexico

ARTICLE INFO

Article history:
Received 29 June 2017
Accepted 19 November 2017
Available online 22 November 2017

Keywords:
Tunneling magnetoresistance
Silicene
Asymmetrical effects
Conductance
Electron transport

ABSTRACT

Electron transport in a silicene structure, composed of a pair of magnetic gates, is studied in a ferromagnetic and antiferromagnetic configuration. The transport properties are investigated for asymmetrical external effects like an electrostatic potential, a magnetic field and for asymmetrical geometric structure. This theoretical study, has been done using the matrix transfer method to calculate the transmission, the conductance for parallel and antiparallel magnetic alignment and the tunneling magnetoresistance (TMR). In Particular, we have found that the transmission, conductance and magnetoresistance oscillate as a function of the width of barriers. It is also found that a best control and high values of TMR spectrum are achieved by an asymmetrical application of the contact voltage. Besides, we have shown that the TMR is enhanced several orders of magnitude by the combined asymmetrical magnetization effect with an adequate applied electrostatic potential. Whereby, the asymmetrical external effects play an important role to improve TMR than symmetrical ones. Finally, the giant TMR can be flexibly modulated by incident energy and a specific asymmetrical application of control voltage. These results could be useful to design filters and digital nanodevices.

1. Introduction

Silicene is a monolayer of silicon atoms, forming a 2D dimensional honeycomb lattice [1–4]. This new material has attracted more attention due to its tremendous application in nanoelectronics and for its special physical properties similar to those of graphene [5–8]. In contrast to graphene, silicene has a large intrinsic spin-orbit interaction and a buckled structure involving valley and spin manipulation [9–13]. Recently, monolayer and multilayer silicene have been synthesized onto metallic substrates as well as a field effect transistor at room temperature reported [6,14].

* Corresponding author.
E-mail address: oubram@uaem.mx (O. Oubram).

https://doi.org/10.1016/j.spmi.2017.11.027
0749-6036/

On the other hand, magnetic fields effects on nanostructures have been proposed to confine massless two-dimensional (2D) Dirac electrons [15–17] as well as a possible route to manipulate electron transport. For instance, Zai and Chang [15] have investigated the spin tunneling magnetoresistance effect in monolayer graphene modulated by two parallel stripes. They found a large TMR ratio of parallel to antiparallel configuration of magnetization and that this ratio can be tuned by the inclusion of an electric field. Likewise, Wang et al. [18] have explored magnetotransport (specifically TMR) in graphene with two tunable magnetic barriers. They have shown that TMR is sensitive to distance between the magnetic barriers. More interestingly, they reported that with asymmetrical barriers, barriers with different height, TMR enhances an order of magnitude with respect to the symmetrical case.

Under this context, silicene is an ideal material to manipulate spin transport due to its intrinsic large spin-orbit coupling. In fact, the scientific community has been committed to improve and control the spin transport properties, particularly magnetoresistance (MR) and TMR [5,19–26]. These properties are quite important for sensors, information, medicine and computer technology [27–29]. For example, Xu et al. [30] have predicted MR up to 1960% in zigzag silicene nano ribbons (ZSiNR) under finite bias voltages. Besides, Kang [31] and collaborators have done a study of the transport properties in ZSiNRs using first principles calculations. They report that the magnetoresistance effect in even-N ZSiNRs can reach 1 000 000%. They proposed that this interesting property could be the basis to design logic gates, such as NOT, AND, and OR on ZSiNRs-based devices. The same system has been analyzed by Zhang et al. [32] under asymmetric edge hydrogenation by means of the nonequilibrium Greens function method and the spin-polarized density functional theory. They found that the resulting giant magnetoresistance can reach 100 000 000%. Their findings could be useful in the development of high performance silicene-based spin filters, spin rectifiers and logic devices.

Recently, Wang et al. [19] suggested the magnetic field as a new path to manipulate valley and spin transport in silicene. They also shown that the conductance and tunneling magnetoresistance, in a silicene structure with ferromagnetic (FM) barriers, can be controlled by magnetic field effects. In specific, they focus on the effect of the asymmetrical magnetization on the valley/spin polarization and TMR. In the same sense, it has been reported that in two ferromagnetic barriers on the top of monolayer silicene [5], magnetic field affects intensively the transmission of the antiferromagnetic (*AFM*) configuration of the device and enlarges the forbidden transmission region for the ferromagnetic case. Qiu et al. [21] analyzed the transport of electrons in FNF silicene junction. They show that a perfect spin and valley polarized conductance can be achieved by adjusting the barrier potential. Likewise, Saxana et al. [22] have investigated the conductance, valley and spin polarization and tunneling magnetoresistance in *FNF* junction of silicene. They found that TMR can be tuned perfectly via electric field effects as well as a fully valley and spin polarized current can be achieved by external field effects.

In this work, we explore electron transport in a silicene structure formed by two ferromagnetic strips. The aim of this study is to investigate asymmetric effects of our system on the transmission, transport and TMR properties. Particularly, we explore the asymmetry between barriers created by means of magnetic and electrostatic fields, bandgap and width of barriers. Our results indicate that the degree of asymmetry can be adjusted to improve the mentioned properties. Specifically, the barriers can be modulated in asymmetric fashion to enhanced the conductance for the parallel configuration of the magnetic field as well as to reduce the anti-parallel one such that the TMR improves several orders of magnitude. We also notice an oscillating behavior of TMR as a function of the barrier width, indicating that resonant tunneling plays an important role in our system. We consider that our results can be valuable to understand electron transport in silicene-based structure and could be useful to design filters and digital silicene-based nanodevices.

2. Theoretical background

The ferromagnetic junction we are interested in, is a nanodevice that basically consists of a silicene sheet and two ferromagnetic strips with different width d_l and d_r separated by a distance L, see Fig. 1a. This device has two ferromagnetic configurations, parallel (*P*) and antiparallel (*AP*). When, the alignment of the strip of right side is same to the alignment to the strip of the left side, the configuration is *P*, see Fig. 1b. In contrast, when they have different alignment, it is *P*, see Fig. 1c.

The control of the Fermi energy of the incident electrons is handled by a delta-type magnetic field (z-coordinate) localized in the edges of the ferromagnetic strips [5,15], see Fig. 1b. The magnetic field B_z, as it is reported in previous works [5,15], is formally described by:

$$B_z(x) = \gamma_l B_l l_{B_0}\left[\delta\left(x + d_l + \frac{L}{2}\right) - \delta\left(x + \frac{L}{2}\right)\right] + \gamma_r B_r l_{B_0}\left[\delta\left(x - \frac{L}{2}\right) - \delta\left(x - d_r - \frac{L}{2}\right)\right], \tag{1}$$

the corresponding magnetic vector potential A is given by $A = [0, A_y(x), 0]$, following the Landau gauge, with $A_y(x)$ deduced from $A_y(x) = \int_{-\infty}^{x} B_z(x)dx$ as

$$A_y(x) = l_{B_0}\left[\gamma_l B_l \Theta\left(x + d_l + \frac{L}{2}\right)\Theta\left(-\frac{L}{2} - x\right) + \gamma_r B_r \Theta\left(\frac{L}{2} + d_r - x\right)\Theta\left(x - \frac{L}{2}\right)\right]. \tag{2}$$

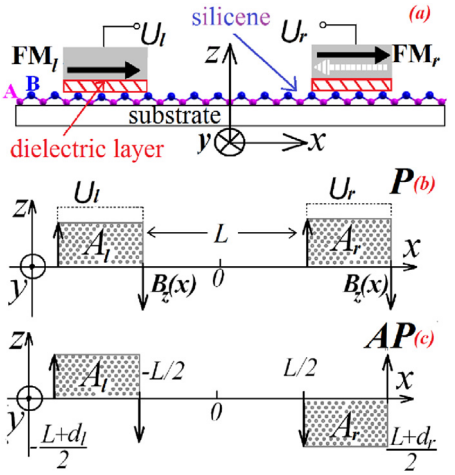

Fig. 1. (a) Schematic representation of the cross section of Ferromagnetic/Normal/Ferromagnetic (*FNF*) asymmetrical junction on the surface of silicene. Silicene consists of buckled honeycomb lattice of silicon atoms with two sublattices A (pink dotes) and B (blue dotes). A typical configuration in such device consists of two ferromagnetic strips (gray rectangles) of specific widths deposited on the top of a thin dielectric layer and separated by a distance L. The width the left strip is d_l and the width of the right one is d_r. Other difference between *FM* gates is the magnetization alignment, the right ferromagnetic gate can have the magnetization in the same direction that the left gate or contrary to it. The magnetization of the left ferromagnetic gate is fixed. Parallel (*P*) (b) and antiparallel (*AP*) (c) magnetization alignments on *FNF* silicene junction are induced by a stray field $B_z(x)$. A_l and A_r are the corresponding transverse magnetic vector potentials (gray rectangles) for *P* and *AP* alignment. Dashed lines in (b) represents the local electrostatic potentials U_l and U_r induced by the top gate voltage. Here, we are interested in the control of the transport properties and consequently the improvement of TMR by structural asymmetrical effects. Specifically, we are considering asymmetrical barriers, in which the contrast is induced by the applied magnetic and electric fields, bandgaps and the width of the barriers. (For interpretation of the references to colour in this figure legend, the reader is referred to the web version of this article.)

here, $\gamma_l = \pm 1$ represent the magnetization of the left *FM* strip (FM_l) parallel $(+1)$ or antiparallel (-1) to x-coordinate, similarly, $\gamma_r = \pm 1$ represent the magnetization of the right *FM* strip (FM_r) parallel $(+1)$ or antiparallel (-1) to x-coordinate, and $l_{B_0} = \sqrt{\hbar/eB_0}$ is the magnetic length, with B_0 a reference magnetic field.

Other flexible strategy to modulate the quantum transport in silicene is to tune the locally electrostatic barrieres (*EBs*) U_l and U_r (see Fig. 1(a) and (b)). The profile of *EB* is given as:

$$U(x) = U_l\Theta\left(x + d_l + \frac{L}{2}\right)\Theta\left(-\frac{L}{2} - x\right) + U_r\Theta\left(\frac{L}{2} + d_r - x\right)\Theta\left(x - \frac{L}{2}\right), \tag{3}$$

where $U_l(U_r)$ is the height of *EBs* induced by $FM_l(FM_r)$ and $\Theta(x)$ is Heaviside function.

Unlike to graphene, silicene is not coplanar [10] and is characterized by a difference in sublattice on-site potential, which results in a local band-gap that can be manipulated by a perpendicular electric field. This local bandgap is considered as [5].

$$\Delta(x) = \Delta_l\Theta\left(x + d_l + \frac{L}{2}\right)\Theta\left(-\frac{L}{2} - x\right) + \Delta_r\Theta\left(\frac{L}{2} + d_r - x\right)\Theta\left(x - \frac{L}{2}\right), \tag{4}$$

where $\Delta_l(\Delta_r)$ is the local bandgap on the ferromagnetic domain $FM_l(FM_r)$. In order to study the transport properties of our system, it is necessary to calculate the band structure.

Silicene under the influence of magnetic and electric fields as well as a local bandgap (ferromagnetic field effects) can be described by the following low-energy effective Hamiltonian around the Dirac point [20].

$$H = \nu_F(\pi_x\tau_x - \eta\pi_y\tau_y) - (\eta\sigma\Gamma_{SO} - \Delta_z)\tau_z + UI, \tag{5}$$

where ν_F is the Fermi velocity of the charge carriers in silicene, $\pi_{x(y)} = P_{x(y)} + eA_{x(y)}$ is the canonical momentum with $P_{x(y)}$ the electron momentum and $A_{x(y)}$ the magnetic vector potential, $\tau = (\tau_x, \tau_y, \tau_z)$ correspond to the sublattice (pseudospin) Pauli matrices, I is the 2×2 matrix unity, $\eta = \pm 1$ denotes the **K** and **K**′ valleys, respectively, and $\sigma = \pm 1$ denotes the spin indices. Γ_{SO} specifies the spin-orbit coupling, which in silicene has a large value 3.9 meV [33]. This is a clear difference with respect to graphene. By solving the eigenvalue equation for this Hamiltonian it is possible to obtain the eigenfunctions and eigenvalues (wave vectors). As our system is composed of different regions (barriers, well and semi-infinite regions) we will have specific wave functions and wave vectors for those regions.

In generic terms we can write the wave function as:

$$\psi_j(x,y) = A_j\begin{pmatrix}1\\ v_j^+\end{pmatrix}e^{+ik_{x,j}x+ik_{y,j}y} + B_j\begin{pmatrix}1\\ v_j^-\end{pmatrix}e^{-ik_{x,j}x+ik_{y,j}y} \tag{6}$$

where

$$k_{x,j} = \sqrt{(E-U_j)^2 - (\eta\sigma\Gamma_{SO} - \Delta_{Z,j})^2 - (k_{y,j}+A_j)^2} \tag{7}$$

and

$$v_j^{\pm} = -\frac{E-U_j+(\eta\sigma\Gamma_{SO}-\Delta_j)}{\pm k_{x,j} + i\eta(k_{y,j}+A_j)}. \tag{8}$$

For the region between the barriers and the semi-infinite regions to the left and right of the barriers $U_j = \Delta_{z,j} = A_j = 0$. The unknown coefficients A_j and B_j are inter-related by the continuity condition at the interface along the x-coordinate

$$\psi_{j+1}(x_{jj+1},y) = \psi_j(x_{jj+1},y), \tag{9}$$

as well as by the conservation of the y component of the momentum

$$k_{y,j} = k_y. \tag{10}$$

The relationship between the coefficients of the left semi-infinite region (A_0 and B_0) and the coefficients of the right semi-infinite one (A_N and B_N) can be write in a more compact form through the transfer matrix, namely

$$\begin{pmatrix}A_0\\ B_0\end{pmatrix} = M\begin{pmatrix}A_{N+1}\\ 0\end{pmatrix}, \tag{11}$$

where the transfer matrix M, given by

$$M = D_0^{-1}\left(\prod_{j=1}^{N} D_j P_j D_j^{-1}\right)D_0, \tag{12}$$

is defined in terms of the dynamic D_j and propagation P_j matrices:

$$D_j = \begin{pmatrix}1 & 1\\ v_j^+ & v_j^-\end{pmatrix} \tag{13}$$

and

$$P_j = \begin{pmatrix}e^{-id_jk_{x,j}} & 0\\ 0 & e^{+id_jk_{x,j}}\end{pmatrix}. \tag{14}$$

Here $j = 1, 2, \ldots, N$. In our case N = 3, represents the first barrier ferromagnetic region, the interwell region and the second barrier. D_0 is the dynamic matrix of the semi-infinite left and right regions, which are the same in this model. Likewise, $k_{x,j}$ and d_j are the x-component of the wave vector and the width of the $j-th$ region, respectively. Knowing the transfer matrix, we can calculate easily the tunneling probability of each scattering channel,

$$t_{P/AP}(E,k_y,\eta,\sigma) = \left|\frac{A_{N+1}}{A_0}\right| = \frac{1}{|M_{11}(\eta,\sigma)|^2}, \tag{15}$$

with the $M_{11}(\eta,\sigma)$ being the first element of the transfer matrix $M(\eta,\sigma)$ for a η and σ representation. The corresponding global quantum transmission in the silicene sheet for a specific magnetization configuration is

$$T_{P/AP} = \frac{1}{4}\sum_{\eta=-1}^{1}\sum_{\sigma=-1}^{1} t_{P/AP}(\eta,\sigma). \tag{16}$$

With the transmission probability at hand, the conductance for a particular spin channel and magnetization can be obtained through the Landauer-Büttiker formula [34]:

$$G_{P/AP}(E_F,\eta,\sigma) = G_0 \int_{-\frac{\pi}{2}}^{\frac{\pi}{2}} t_{P/AP}(E_F,\theta,\eta,\sigma)\cos(\theta)d\theta. \tag{17}$$

The global conductance according to the alignment is

$$G_{P/AP}(E_F) = \frac{1}{4}\sum_{\eta=-1}^{1}\sum_{\sigma=-1}^{1} G_{P/AP}(E_F,\eta,\sigma), \tag{18}$$

where E_F is the Fermi energy, $G_0 = e^2 L_y k_F/\pi^2\hbar$ is the fundamental conductance factor with L_y being the width of the system in the transversal y-coordinate, $k_F = \sqrt{E_F^2 - \Gamma_{SO}^2}$ is the Fermi wave-vector, and θ is the angle of incident electrons with respect to the x-coordinate, given by the relation between the transversal wave vector and the Fermi wave vector $k_y = k_F\sin(\theta)$.

Once the conductance is computed TMR for specific spin and valley channels can be obtained through the following expression:

$$TMR(\eta,\sigma) = \frac{G_P(\eta,\sigma) - G_{AP}(\eta,\sigma)}{G_{AP}(\eta,\sigma)}. \tag{19}$$

Equivalently, the global TMR is given by,

$$TMR = \frac{G_P - G_{AP}}{G_{AP}}. \tag{20}$$

3. Numerical and theoretical results

We now apply the above formulation to calculate the transmission, conductance and TMR of Dirac fermions on the silicene structure for parallel and antiparallel alignment. The structure consists of a quantum well and ferromagnetic barriers of widths d_w, d_l and d_r, respectively. An asymmetrical system or asymmetrical barriers can be obtained by having a contrast (difference) between the magnetic fields, the electrostatic potentials, the local bandgaps and the widths between the left and right barrier. In order to understand all these asymmetrical possibilities we will analyze them individually, that is, we will vary one of them by keeping all other constant. Other aspect that it is important to mention is the relevance of the valley and spin degrees of freedom. So, we have four transmission and transport channels, two (spin up and down) per valley (K and K′).

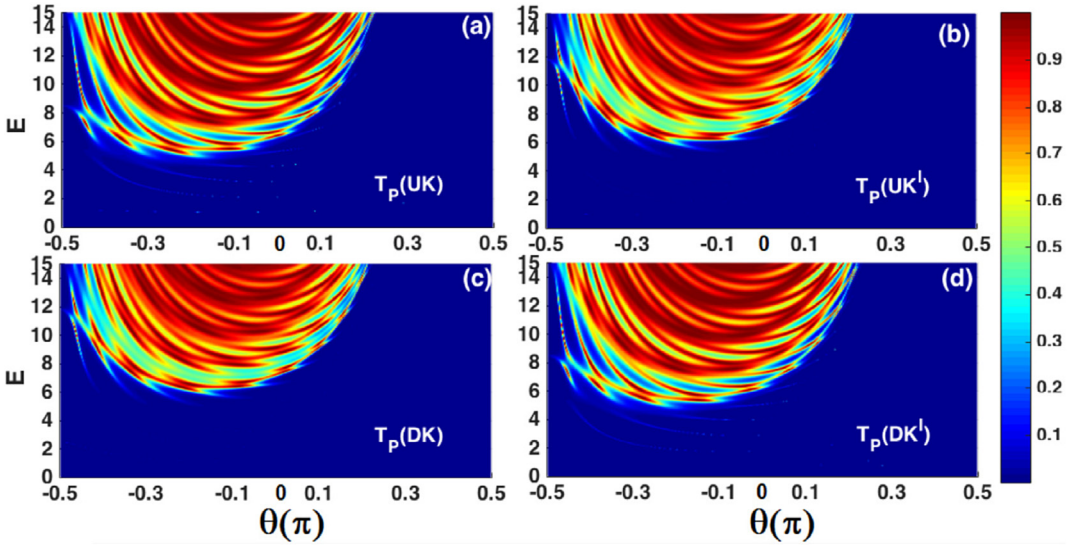

Fig. 2. Parallel transmission (T_P) as a function of the energy and the angle of incidence for: (a) and (b) the spin-up component in the K and K′ valley; and (c) and (d) the spin-down component in the K and K′ valley. Here, $U_l = U_r = 2$, $B_l = B_r = 3$, $\Delta_l = 0$, $\Delta_r = 3$ and $d_l = d_r = \frac{l}{2}$.

The first asymmetrical aspect that we will analyze is the one related to the local bandgap ($\Delta_l \neq \Delta_r$). Specifically, we are considering a local bandgap of $\Delta_l = 0$, and $\Delta_r = 3$ for the left and right barrier, respectively, by keeping all other parameters constant, namely: $B_l = B_r = 3$, $U_l = U_r = 2$, $d_w = L$ and $d_l = d_r = L/2$. In Fig. 2 we show our outcomes for the transmission probability or transmittance in the case of the parallel configuration of the magnetic field (T_P). Fig. 2a–d correspond to transmission contours as a function of the energy and angle of incidence for the spin-up component in the K and K′ valleys (T_P(UK) and T_P(UK′)) and the spin-down component in the K and K′ valleys (T_P (DK) and T_P (DK′)), respectively. As we can see in practically all contour plots there are a plethora of electron states, from propagating states (red regions) to forbidden ones (deep blue regions), depending on the energy and angle of incidence. We can also notice that the spin-up and spin-down components of the transmittance for the same valley have different characteristics. For instance, we can see that even when the negligible transmission region is nearly the same in both components the non negligible regions have different branches with different degrees (probabilities) of transmission. It is also noted a similarity of the transmission components between valleys. In specific, the transmission map of the spin-up component in the K valley (Fig. 2a) is nearly the same that the transmission map of the spin-down component in the K′ valley (Fig. 2d). The same applies for T_P (DK) and T_P(UK′), Fig. 2c and b, respectively. This similarity can be understood by taking into account the component of the wave vector in the propagation direction k_{xj}, see eq. (7), and more precisely by realizing that the term $\eta\sigma$ is the same for T_P(UK) and T_P (DK′) as well as for T_P (DK) and T_P(UK′). As we already mentioned the two barriers are practically transparent, propagating states, for different energies and angles of incidence. This effect is a result of the confabulation of resonance conditions, Fábry-Perot resonances, in the well region and the left and right barriers. It is also important to remark that the transmission gap reaches almost $E = 5$. Moreover, the transmission domain is stretched to the left, mainly due to the magnetic field effects.

For *AP* alignment we can see that the non negligible transmission domain is greatly reduced, whence, the forbidden zone increases, see Fig. 3. In addition, the transmission gap rises beyond of a critical value of incident energy $E > 6$. As in the case of parallel alignment, the contour plot for T_{AP}(UK) is similar to the corresponding one for T_{AP} (DK′), Fig. 3a and d, the same applies for T_{AP} (DK) and T_{AP}(UK′), see Fig. 3c and b. As we already mentioned this similarity comes from the equivalence of the wave vectors between the these components. If we see in more detail the contours, they are not totally equivalent, in fact the differences that we can notice are a result of the discrepancies in the components of the wave functions between the mentioned transmission channels. Another important characteristic of the transmission maps is a mild asymmetry around $\theta = 0$ toward the left. Precisely, this asymmetry is due to the asymmetrical effect of the local bandgap $\Delta_l \neq \Delta_r$. At this point, it also is important to mention that the reduction of the AP transmission could be beneficial for TMR since this quantity (TMR) can be improved by reducing the antiparallel component of the conductance as well as by enhancing the parallel one.

Here, it is important to remark that TMR is a preponderant quantity due to its physical significance and technological implications. This quantity depends directly on the conductance characteristics for parallel and *anti*-paraller configurations. Then, in order to understand TMR results we firstly show and analyze the conductance characteristics for the mentioned configurations as well as for the different spin and valley components. In Fig. 4, the *P* conductance (G_P) and *AP* conductance (G_{AP}) for the four dispersion channels as a function of the Fermi energy are shown. We can notice that G_P and G_{AP} tends to 0, when the Fermi energy is below a critical value $E_F < 5$ and $E_F < 6$, respectively. Thereupon, it tends to grow in an oscillatory

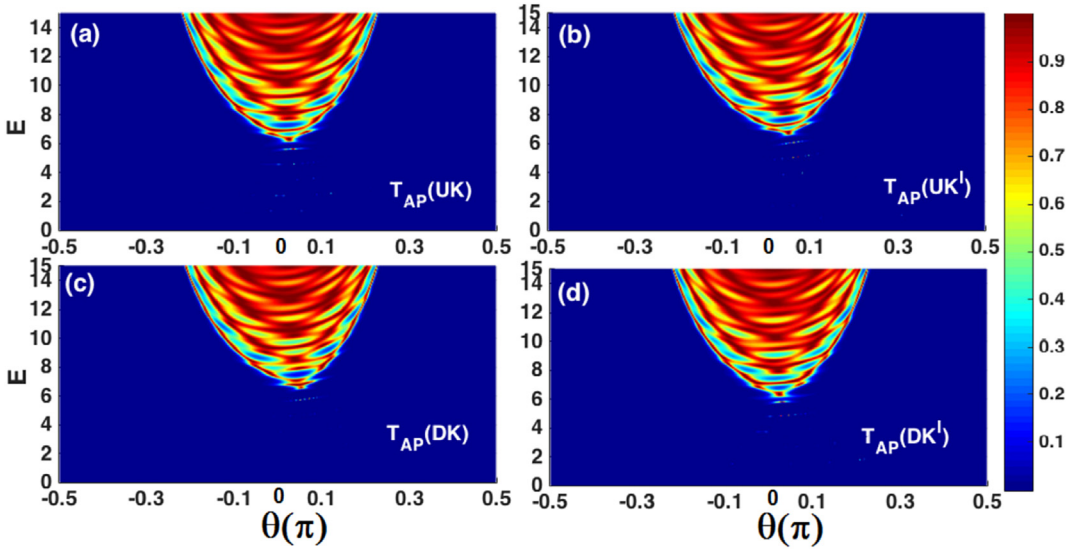

Fig. 3. Contours of the antiparallel transmission T_{AP} as a function of the energy and the angle of incidence for the different spin components and valleys. (a) and (c) correspond to the spin up and down components for the K valley, T_{AP}(UK) and T_{AP} (DK), respectively, while (b) and (d) correspond to the spin up and down components for the K′ valley, T_{AP}(UK′) and T_{AP} (DK′), respectively. Here, $U_l = U_r = 2$, $B_l = B_r = 3$, $\Delta_l = 0$, $\Delta_r = 3$ and $d_l = d_r = \frac{L}{2}$.

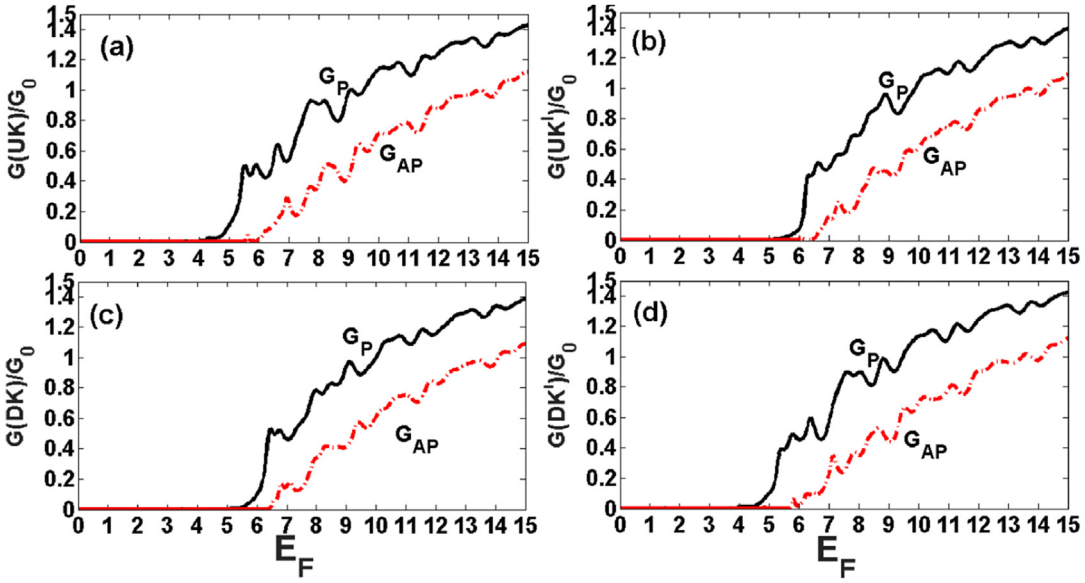

Fig. 4. Parallel (G_P) and antiparallel (G_{AP}) conductance as a function of Fermi energy E_F. (a) and (c) correspond to the spin-up and spin-down channels in the K valley, while (b) and (d) to the same channels but in the K′ valley. In this case the asymmetry comes from the difference between the left and right local bandgaps, $\Delta_l = 0$ and $\Delta_r = 3$. The other parameters are $U_l = U_r = 2$, $B_l = B_r = 3$ and $d_l = d_r = L/2$. The solid and dashed lines correspond to G_P and G_{AP}, respectively.

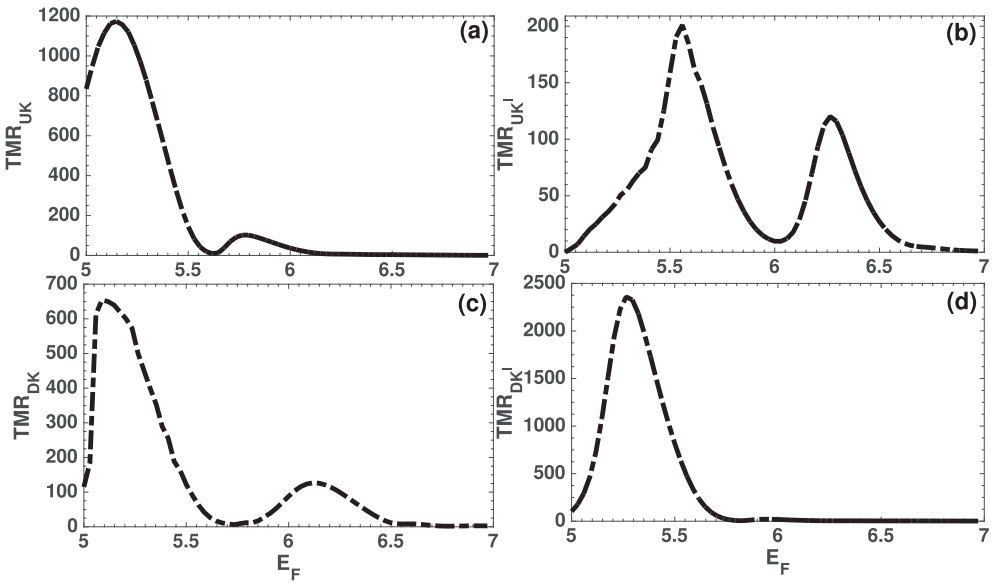

Fig. 5. TMR ratio versus Fermi energy for channels (a) UK, (b) UK′, (c) DK and (d) DK'. The asymmetry in our system is provided by the difference between the local bandgaps between the left and right barriers, $\Delta_l = 0$ and $\Delta_r = 3$. The other parameters of our structure are the same as in Fig. 4.

way. The oscillations are due precisely to the resonances shown in Figs. 2 and 3. We can also notice that as the energy increases the difference between the *P* and *AP* conductance is keeping at the same order of magnitude and at the same time the *AP* conductance increases. This trend is not beneficial for TMR because this quantity is inversely proportional to the *AP* conductance. The best scenario for TMR is that the parallel component of the conductance be maximize and the anti-parallel one be minimized. That is a hard task, so other possibilities are welcomed. A reasonable option is to keep *P* conductance at good levels and at the same time to diminish *AP* conductance as much as possible, under detectable levels. Under this context the energy range of interest is $5 < E < 7$. Wherein, G_{AP} is evanescent and G_P is finite. In Fig. 5 we show our results for TMR in the mentioned range $5 < E < 7$. Fig. 5a and c correspond to the spin-up and spin-down components in the K valley, while Fig. 5b and d represent our outputs for the spin-up and spin-down components in the K′ valley. We can notice that TMR is not equivalent for the different channels as well as *UK* and *DK′* channels are dominant. In fact, the maximum TMR value for these

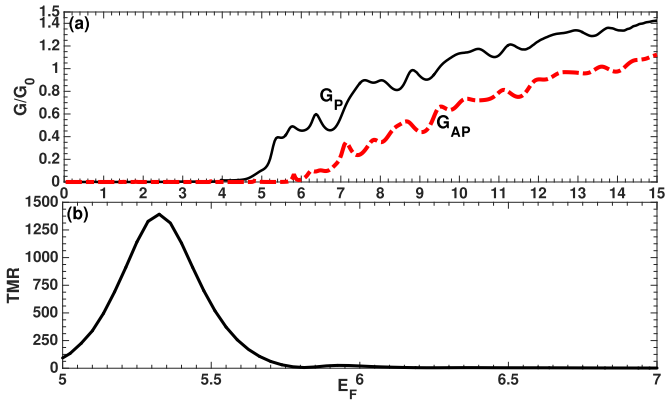

Fig. 6. (a) Global conductance as a function of Fermi energy E_F. The solid-black and dashed-red lines correspond to G_P and G_{AP}, respectively. (b) Global TMR versus the Fermi energy. The asymmetry in our system is provided by the difference between the local bandgaps between the left and right barriers, $\Delta_l = 0$ and $\Delta_r = 3$. The other parameters of our structure are the same as in Figs. 4 and 5. (For interpretation of the references to colour in this figure legend, the reader is referred to the web version of this article.)

dominant channels is nearly 7 times the maximum TMR value for *DK* and *UK′* channels. Thereby, the overall conductance is mainly determined by the dominant channels, see Fig. 6a. In this figure we also show the global conductance for the parallel and anti-parallel configurations. As we can see global conductances are similar to the conductances of the different channels. However, in this case the energy range for which G_{AP} is evanescent and G_P is finite is reduced to $5 < E < 5.5$, which corresponds to the energy range for maximum TMR, see Fig. 6b. Precisely, this figure presents the global TMR, which is shaped by the dominant channels.

Now it is turn to analyze another effect that can make our system asymmetric, namely electrostatic field effect. Specifically, we will consider electrostatic potentials in the left and right barriers applied in asymmetric fashion, that is, the left and right electrostatic potentials will have a contrast. As in the case of the local bandgap we will show and analyze the transmission and transport properties in order to understand in a better way TMR characteristics. We can also carry out a similar analysis for the different spin components and valleys, however instead of doing that, we will show our global results for different potential strengths. In Figs. 7 and 8 we show the transmission contours for *P* and *AP* configurations as a function of the angle of incidence θ and the height of the right barrier for different strengths of the left barrier: (a) $U_l = 2$, (b) $U_l = 4$, (c) $U_l = 6$ and (d) $U_l = 7$. The Fermi energy has been kept fixed at $E_F = 5$. As we can see there is a high anisotropy in practically all the transmission maps. The anisotropy in the angular part is caused by the shifting of the Dirac cones in the barrier region due to the applied magnetic field. In Fig. 7 we can also notice that the active region of T_P is reduced as U_l is closed to $E_F = 5$, see Fig. 7b and c. This reduction is a consequence of the wave vector filtering. Specifically, when the height of U_l approaches to the Fermi

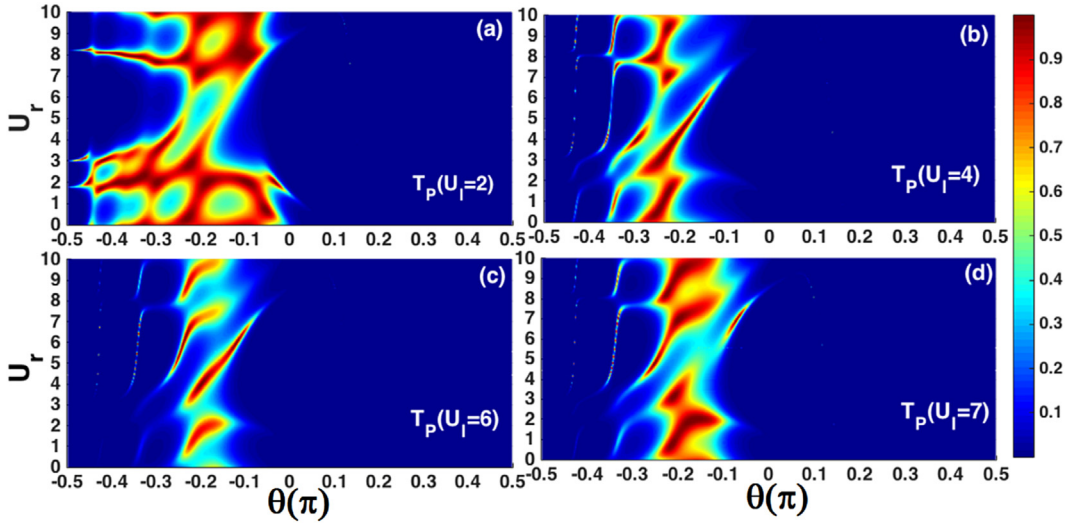

Fig. 7. Transmission maps for parallel alignment. The coordinates of the maps are the angle of incidence and the height of the right electrostatic barrier U_r. Different heights of the left barrier have been considered: (a) $U_l = 2$, (b) $U_l = 4$, (c) $U_l = 6$ and (d) $U_l = 7$. Here, $B_r = B_l = 3$, $E_F = 5$, $\Delta_l = \Delta_r = 0$ and $d_l = d_r = \frac{l}{2}$.

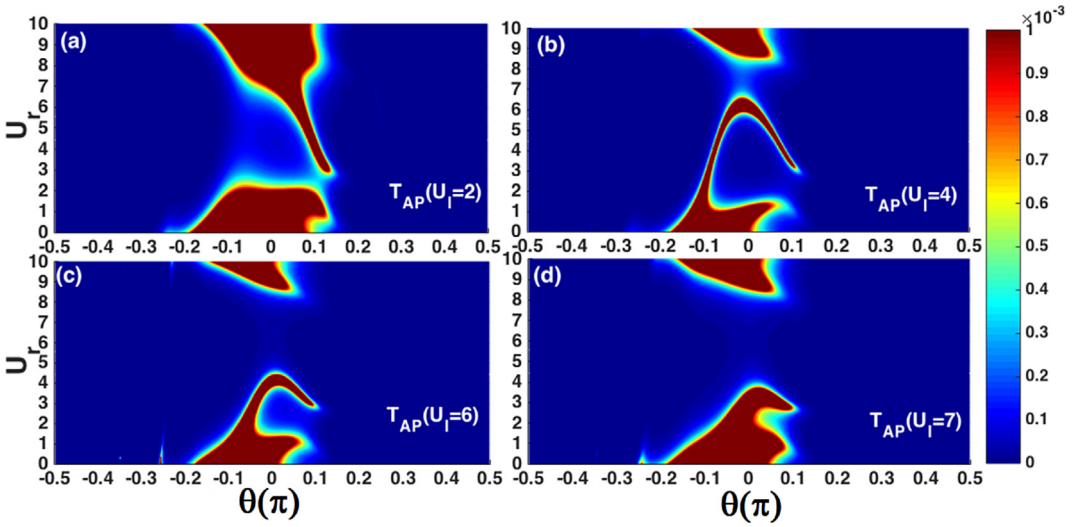

Fig. 8. The same as in Fig. 7, but for the antiparallel configuration.

energy (E_F=5), the character of electrons changes from propagating to evanescent (see Eq. (7)). It is also important to mention that we can find resonant states in practically all transmission maps, however for $U_l = 2$ these states become preponderant around $U_r = 2$ and $U_r = 8$, that is, they covered an important angular range. In the case of the antiparallel configuration we can see that for different U_l the T_{AP} spectrum diminish drastically, 3 orders of magnitude. As we can notice the change in the magnetic field alignment gives rise to totally different transmission maps. In particular, most of the transmission contours are dominated by negligible transmission probability regions. The high transmission regions, associated to resonant states, correspond to small angles as well as to high and low U_r. It is also worth noting that the high transmission regions are separated by a transmission bandgap, which is enlarged as U_l increases. This reduction of the transmission properties for *AP* alignment in conjunction with the high transmission regions for *P* alignment will determine the TM characteristics.

In order to better understand the transmission results, we investigate the conductance G_P and G_{AP} as a function of U_r, see Fig. 9. From this figure we see that G_P is almost symmetric around $U_r = 5$. In fact, it drops monotonically with U_r until reaches a minimum value around $U_r = 5$. Afterward, it increases with U_r, see Fig. 9a. Whereas, G_{AP} drops monotonically, but it stays finite and then increases with U_r, see Fig. 9b. Moreover, G_P and G_{AP} decrease as U_l increases (U_l=2,4,5), afterward tend to increase as $U_l > 5$. This behavior can be explained by the parity of k_x function around $E_F = 5$ (see Eq. (7)), where $k_x(U_{r(l)} - E_f) = k_x(-(U_{r(l)} - E_f))$. Another important characteristics is that G_P exhibits oscillatory behavior with pronounced amplitude close to $U_r = 2$ and $U_r = 8$. This behavior is originated by the resonance phenomena manifested at $U_r = 2$ and 8 (see Fig. 7), which highly intensified for $U_l = 2$. Then the amplitude of G_P conductances can be controlled perfectly by U_r or U_l. In the case of G_{AP} a wide forbidden region is presented. This region comes from the dominant evanescent mode for $E - B < U_{r(l)} < E + B$, where in this domain the electron transmission is blocked by high left barrier. In contrast, we note a localized resonance peaks at different heights of the right barrier. For instance, for $U_l = 4$ the peak is localized at $U_r = 6$. Precisely, this manifestation is expected from Fig. 8b, where, a resonance channel for $U_l = 4$ is manifested at $U_r = 6$. The same behavior is observed for $U_r = 3.4$, 4 and 5, see Fig. 9b and c.

Now it is turn to analyze how G_P and G_{AP} shape TMR. As in the preceding cases we show TMR as a function of U_r for different heights of the left barrier U_l, see Fig. 10. We can notice that the suppression of the left electrostatic barrier induces TMR peaks localized at low U_r (see the inset in Fig. 10). This is a consequence of the transmission blocking of *AP* alignment, whereby, it is dominant in the low field domain. Similar result is reported by Zhai and Chang in graphene [15]. Additionally, we notice that TMR has a blue shifting for $U_l \leq 4$, while a red shifting is presented for $U_l \geq 5$. We can also see that TMR can be practically null for different values of U_r as well as that those regions for negligible TMR can be modulated by changing the height of the left barrier. Here, it is also important to remind the other values that we are considering as the Fermi energy $E_F = 5$, the magnetic field in the left and right barriers $B_l = B_r = 3$, and the local bandgaps $\Delta_l = \Delta_r = 0$ have an impact in the nature of the wave vector. Actually, for the specific values of these parameters the wave vector argument is complex in both barriers. Physically, it means that the propagation mode is suppressed in both barriers. The same behavior is noted around $U_r = 4.5$ for $U_l = 6$ and $U_r = 3$ for $U_l = 7$ (see Eq. (7)). At this point is important to remark that the asymmetry caused by having a contrast between the heights of the left and right barrier really improves TMR. In fact, as we can notice the maximums for TMR do not correspond to symmetric barriers $U_l = U_r$. For instance, for $U_l = 2$ and $U_l = 5$ the peaks are localized at $U_r = 3$ and $U_r \simeq 6.8$, respectively. Furthermore, the active region of TMR, the non zero region of TMR, is larger as U_l increase. This feature is consequent of the maximization of wave vector filtering mechanism as U_l increases. It means that the width of the TMR active

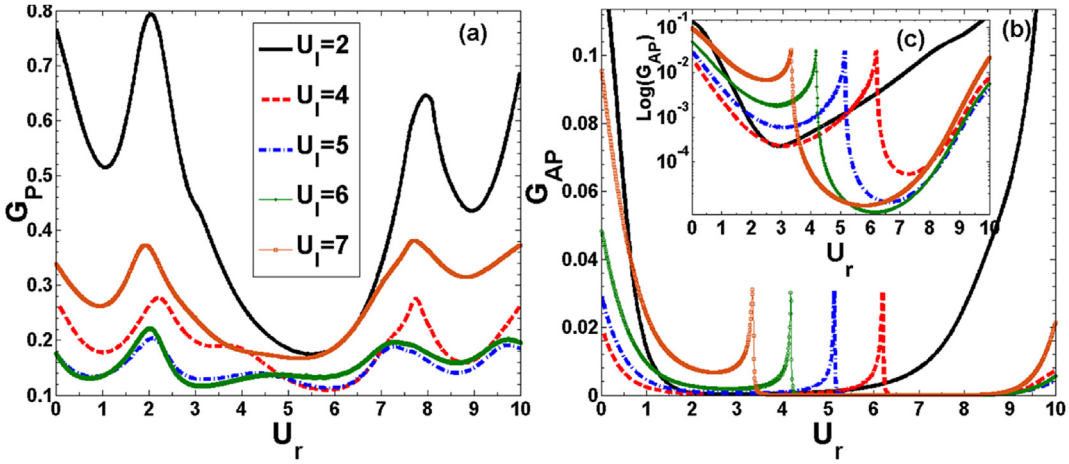

Fig. 9. (a) Parallel conductance G_P and (b) antiparallel conductance G_{AP} as function of U_r. Different values for U_l have been considered, specifically: $U_l = 2$, 4, 5, 6 and 7. The other parameters are the same as in the cases of parallel and antiparallel transmission contours, Figs. 7 and 8. The inset (c) corresponds to G_{AP} in logarithmic scale.

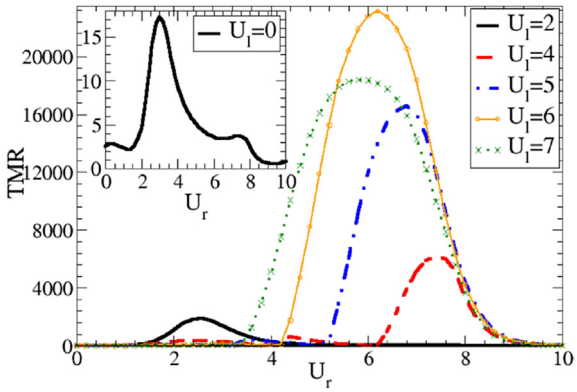

Fig. 10. TMR ratio as a function of U_r for different U_l, namely: $U_l = 0$, 2, 4, 5, 6, 7. The Fermi energy, the magnetic fields and the local bandgaps in the left and right barriers are the same as in Fig. 9. The inset shows the variation of TMR for $U_l = 0$.

region depends on the strength of the left electrostatic barrier U_l. In other words, this dependence is caused by the change of the T_{AP} gap induced by U_l (see Fig. 8).

As we have corroborated external voltages applied in asymmetrical fashion are a perfect tool to modulate the transmission, transport and TMR properties. These properties can be improved by fixing U_l and tuning U_r. Then asymmetrical applied voltages represent an additional strategy to control the transport properties of nanoelectronics based in silicene.

To better understand the effect of U_r on the transport properties, we have computed *P* and *AP* conductances as well as TMR versus the applied voltage U_r and incident energy *E*, see Fig. 11. Qualitatively, for energy below a critical value ($E < 4$), G_P is attenuated for all U_r. Besides, G_{AP} is attenuated in practically all the energy and U_r range considered, except for high energy and low U_r. These characteristics will have a huge impact on TMR. In fact, we obtain a giant TMR (more than 10^4) around $E = 4.5$ and $E = 3.5$, see Fig. 11c. This indicate that giant TMR can be flexibly manipulated by the gate voltage U_r while keeping the energy constant, or vice versa.

Now it is turn to analyze the asymmetry that can be obtained by applying non-equivalent magnetic field to the left and right barriers. In Fig. 12 we show the conductance for both alignment with respect to the right magnetic barrier for different electrostatic barriers: $U_l = U_r = 2,3,6,7$. In Fig. 12a we can see that G_P has a symmetrical behavior around a critical value between $B_r = 2$ and $B_r = 3$. This characteristic is presented irrespective of the strength of the electrostatic barriers. We can also notice that as the strength of electrostatic barriers increases G_P diminishes in general. This trend is presented for most barrier strengths considered, except for $U_r = U_l = 7$. This mechanism is expected by the physical parity of the wave vector k_x around $E_F = 5$ (see Eq. (7)). In Fig. 12b the results for G_{AP} are shown. In this case the conductance presents a decreasing trend as B_r increases. Other important aspect to notice is that G_{AP} is various orders of magnitude lower than G_P, observe the logarithmic scale for G_{AP}. The rising of the electrostatic barriers causes a similar effect as in the case of the parallel conductance, that is, G_{AP}

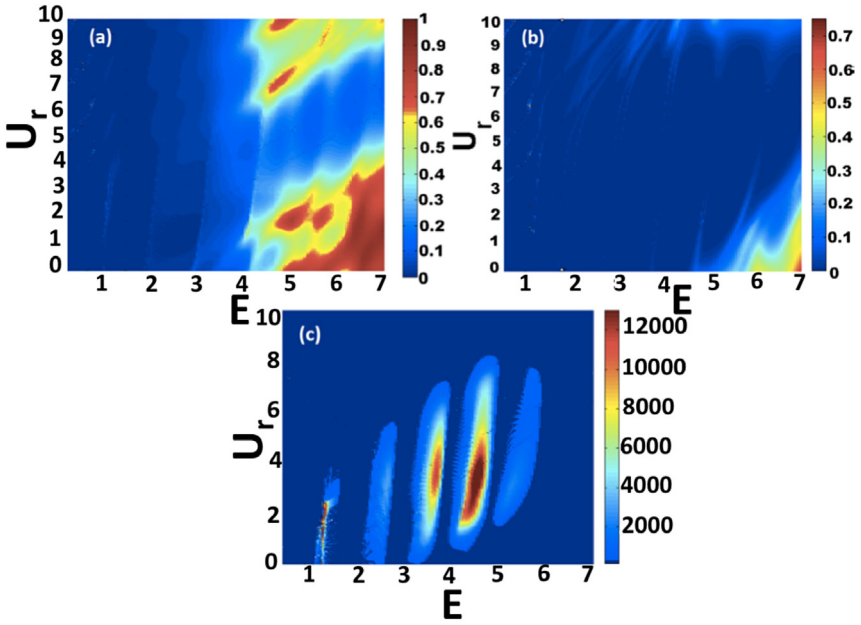

Fig. 11. The incident energy E and the right contact voltage U_r-dependent (a) parallel conductance G_P and (b) antiparallel conductance G_{AP}. The effect of E and U_r on (c) tunneling magnetoresistance TMR. The results are evaluated at $B_l = B_r = 3$, $\Delta_l = \Delta_r = 0$ and $U_l = 2$.

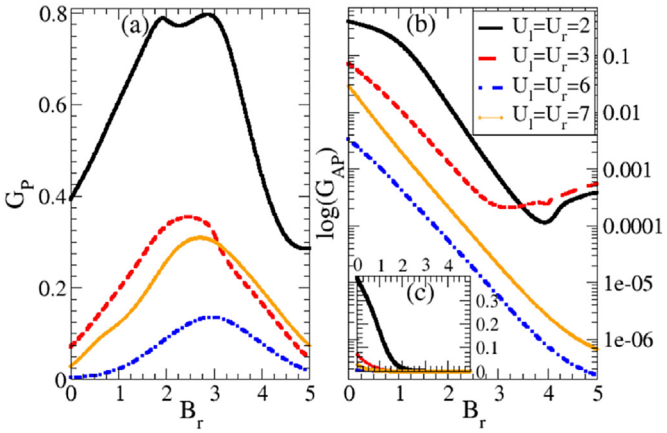

Fig. 12. Linear-regime conductance for (a) parallel alignment G_P and (b) antiparallel alignment G_{AP} versus the right magnetic barrier B_r for different electrostatic barriers, in specific $U_l = U_r = 2, 3, 6, 7$. In this case, we have considered $E_F = 5$, $B_l = 3$ and $\Delta_l = \Delta_r = 0$. The inset is for linear quantum conductance for antiparallel alignment G_{AP}.

decreases monotonically, expect for $U_r = U_l = 7$. An important parameter to understand this transport characteristics is the transversal wave vector. Actually, by incorporating a magnetic field the transversal wave vector is modified by a term that is proportional to the magnetic field strength. More explicitly, we are pinning up $B_l = 3$ and varying B_r. By increasing the B_r from 0 to 5, the transversal wave vector of the antiparallel alignment intensifies. This induces a blockage of the carriers that propagate to the second barrier. Hence, the G_{AP} declines strongly. In the parallel alignment case, the wave vectors difference between both magnetic barriers decreases from $B_r = 0$ to $B_r = 3$. Hence, the propagating modes in this domain will be favoured and consequently G_P will be enhanced. On the other hand, the decrement of G_P from $B_r = 3$ to $B_r = 5$ is due to the intensification of the transversal wave vector difference between both barriers. In other words, the decrement is a result of magnification of evanescent modes in this region ($3 < B_r < 5$).

As consequence of the variation of G_P and G_{AP} with B_r for different strengths of the electrostatic barriers, the TMR peak is increased several orders of magnitude, see Fig. 13. By introducing the asymmetric magnetic field effect, it is observed that TMR increases at various orders of magnitude, note the peak at $B_r = 3$ for $U_l = U_r = 3$ and at $B_r = 4.5$ for $U_l = U_r = 6$. As we can see TMR is enhanced 3 to 5 orders of magnitude. In addition, the magnitude and the region of operation can be controlled by

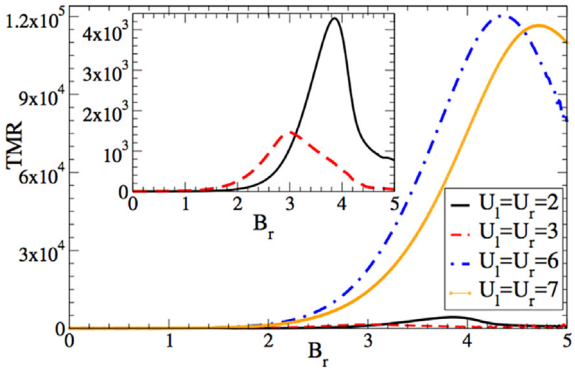

Fig. 13. TMR ratio as a function of B_r for different strengths of the electrostatic barriers, namely, $U_l = U_r = 2, 3, 6, 7$. In this case $E_F = 5$, $B_l = 3$ and $\Delta_l = \Delta_r = 0$. The inset shows the variation of TMR for $U_l = U_r = 2, 3$.

changing the strength of the magnetic and electrostatic barriers. In fact, we find that TMR reaches more than 10^5 for $B_r = 4.5$ (asymmetrical case $B_l \neq B_r$), which represents 10 times the TMR value for the symmetrical case (B_l=$B_r = 3$). In this case the electrostatic barriers are fixed at $U_l = U_r = 6$. Then, as we have corroborated by adjusting the magnetic barriers in asymmetrical fashion as well as appropriately choosing the electrostatic barriers TMR can be improved significantly, more than 3 orders of magnitude. It is also important to remark that this enchantment is not reported previously in silicene structures. This property could be of great importance in the silicene-based sensor and nanodevices industry where high TMR values are required.

Up to this point, we have testified that regardless of the simplicity of a double barrier system, it has a set of asymmetric possibilities that can be exploited to improve TMR. So far we have studied external asymmetrical effects, however there is another possibility related to the structural characteristics of the device. In specific, the width of the barriers represents another option of asymmetry. So, we have studied the transmission of both configurations depending on the size of the right barrier d_r and fixing the left one (d_l=$\frac{L}{2}$). In Fig. 14, we show the transmission maps of the parallel and antiparallel configurations. The vertical axis corresponds to the width of the right barrier, while the horizontal axis to the angle of incidence. The panels of the left and right column correspond to T_P and T_{AP}, while first and second row to $U_l = U_r = 0$ and $U_l = U_r = 2$, Fig. 14a–d, respectively. As we can notice the change in the alignment has a significant impact on the transmission properties. In particular, the transmission is reduced drastically in most parts of the transmission map, being different from zero at regions close to normal incidence, $\theta = 0$. By changing from parallel to antiparallel alignment the transmission landscape is

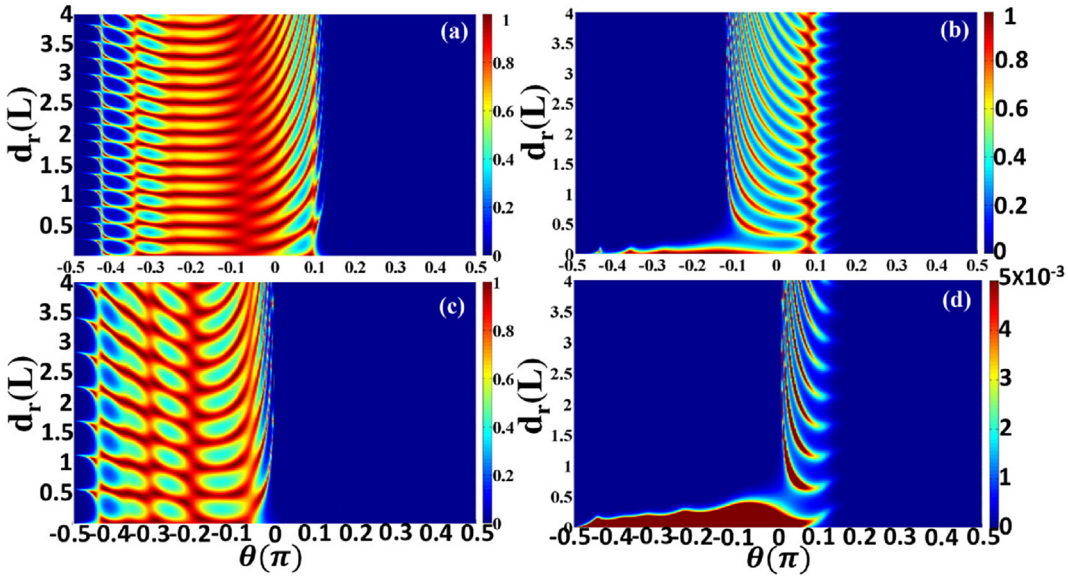

Fig. 14. Transmission maps for (a) (c) parallel and (b) (d) antiparallel alignment. In this case the coordinates of the maps are the width of the right barrier (vertical axis) and the angle of incidence (horizontal axis). Two height of the electrostatic barriers have been considered: (a) (b) $U_l = U_r = 0$ and (c) (d) $U_l = U_r = 2$, respectively. The other parameters are: $d_l = L/2$, $B_r = B_l = 3$, $E_F = 5$ and $\Delta_l = \Delta_r = 0$.

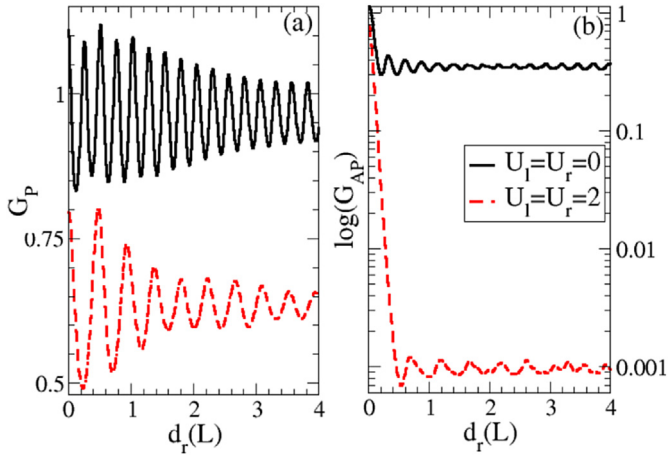

Fig. 15. (a) Parallel and (b) logarithm antiparallel conductance as a function of d_r for two different heights of the electrostatic barriers, $U_l = U_r = 0$ and $U_l = U_r = 2$, solid-black and dashed-red curves, respectively. The other relevant parameters come as: $d_l = L/2$, $E_F = 5$, $B_l = B_r = 3$ and $\Delta_l = \Delta_r = 0$. (For interpretation of the references to colour in this figure legend, the reader is referred to the web version of this article.)

changing from a dominant propagating mode to a dominant evanescent mode. Likewise, by increasing the height of the electrostatic barriers an extra reduction takes place for both alignments. This reduction comes from the filtering of the wave vector (see Eq. (7)) as $U_l = U_r$ increases. An even more interesting characteristic, it is the periodic pattern of the transmission that is presented as a function of d_r. Actually, the barriers are resonant cavities, so a change in its width also represents a change in the resonant condition. In the case of $U_l = U_r = 0$ the patterns are spaced closely for both T_P and T_{AP}, while for $U_l = U_r = 2$ the space between the patterns is enlarged. In other words the period of the patterns can be modulated by the electrostatic barriers. Interestingly, the same resonance periodicity has been observed in structures based on graphene [35]. Specifically, the periodicity is induced when the relation $k_x D_r = n\pi$ is fulfilled. On the same footing, we can confirm that the periodicity arises when the resonant condition $k_x d_r = n\pi$ is established. Here, it is also important to mention that as the wave vector depends on height of electrostatic barriers, then a change in $U_r = U_l$ also implies a change in the resonant condition, and hence a change in the period of the transmission patterns. As the conductances as well as TMR depend directly on the transmission properties it is expected that these quantities also present a periodic dependence with respect to the barrier width.

In Fig. 15 we show the conductance for the parallel and antiparallel alignment as a function of d_r for two different values of the electrostatic barriers, $U_l = U_r = 0$ and $U_l = U_r = 2$, solid-black and dashed-red curves, respectively. As we can see both conductance configurations have an oscillating behavior. We can also notice that a damping is taking place as the barrier width increases, that is, the amplitude of the oscillations diminish as d_r grows. In addition, the conductances diminish as the electrostatic barriers grow, being more dramatic the reduction for G_{AP}, consider the logarithmic scale for this configuration. Here, it is also worth mentioning that our results agree with the oscillations obtained in normal/ferromagnetic/normal silicene junctions [20]. In fact, these oscillations are attributed to the anomalous tunneling of massless Dirac fermions [20,35].

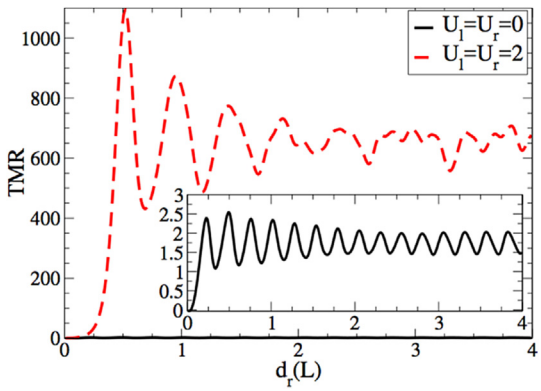

Fig. 16. TMR ratio as a function of d_r for two different heights of the electrostatic barriers, $U_l = U_r = 0$ and $U_l = U_r = 2$, solid-black and dashed-red curves, respectively. The other relevant parameters of the system are the same as in Fig. 15. The inset shows the variation of TMR for $U_l = U_r = 0$. (For interpretation of the references to colour in this figure legend, the reader is referred to the web version of this article.)

In Fig. 16 we present TMR as function of the size of the right strip d_r for two values of the electrostatic barriers, $U_l = U_r = 0$ and 2, solid-black and dashed-red curves, respectively. As we can see the oscillating-damping behavior of the conductances is also reflected in TMR. Likewise, TMR for $U_l = U_r = 2$ is larger, by 3 orders of magnitude, than for $U_l = U_r = 0$. This results is a consequence of the reduction of G_{AP}, several orders of magnitude, as the electrostatic barriers grow. In addition, we notice that the dominant TMR peak is located at $d_r = \frac{L}{2}$ for $U_l = U_r = 2$, which corresponds to the resonant conditions between the barriers $d_l = d_r = L/2$. In short, the asymmetry provided by non equivalent barrier widths, in conjunction of an appropriate election of the other relevant effects in the system such as the electrostatic and magnetic fields as well as the local bandgap, can help to improve TMR characteristics.

4. Conclusions

In summary, we have investigated the electron transport in double magnetic barrier on the top of silicene monolayer in ferromagnetic and antiferromagnetic configuration. The transport properties have been studied under asymmetrical electrostatic potential and magnetic field for asymmetrical geometrical structure. The results indicated the asymmetric applied voltage along with incident energy can tuned the TMR spectrum. Furthermore, the combined asymmetrical magnetization effect with an adequate electrostatic potential can enhance TMR up to more than three orders of magnitude. Particularly, we have shown also that the effect of asymmetric magnetization improves the TMR more than two orders of magnitude compared with the symmetrical effect. Finally, we found the increase of the degree of asymmetric barriers does not contribute on the enhancing of TMR, but, it produces oscillatory phenomena of TMR and conductivity, due to the resonance periodicity behavior of transmission. This finding is highlighted in graphene and silicene structure ref. [20,35]. We hope ours results will guide experiment efforts to development of the silicene-based sensor and nanodevices industry where high TMR values are required.

Acknowledgments

This work was partially supported by PAPIIT-IN104616 from UNAM and CONACYT-252677.

References

[1] K. Takeda, K. Shiraishi, Phys. Rev. B 50 (1994) 14916.
[2] P. De Padova, P. Vogt, A. Resta, J. Avila, I. Razado-Colambo, C. Quaresima, et al., Appl. Phys. Lett. 102 (2013) 163106.
[3] P. De Padova, J. Avila, A. Resta, I. Razado-Colambo, C. Quaresima, C. Ottaviani, et al., J. Phys. Condens. Matter 25 (2013) 382202.
[4] T. Aizawa, S. Suehara, S. Otani, J. Phys. Chem. C 118 (2014) 23049.
[5] Y. Wang, Y. Lou, J. Appl. Phys. 114 (2013) 183712.
[6] L. Tao, et al., Nat. Nanotech 10 (2015) 227.
[7] Z. Ni, Q. Liu, K. Tang, J. Zheng, J. Zhou, R. Qin, et al., Nano Lett. 12 (2012) 113.
[8] K. Zberecki, M. Wierzbicki, J. Barna, R. Swirkowicz, Phys. Rev. B 88 (2013) 115404.
[9] X.L. Qi, S.-C. Zhang, Phys. Today 63 (2010) 33.
[10] N.D. Drummond, V. Zólyomi, V.I. Fal'Ko, Phys. Rev. B 85 (2012) 075423.
[11] J. Linder, T. Yokoyama, Phys. Rev. B 89 (2014) 020504 (R).
[12] N. Missault, P. Vasilopoulos, V. Vargiamidis, F.M. Peeters, B. Van Duppen, Phys. Rev. B 92 (2015) 195423.
[13] V. Vargiamidis, P. Vasilopoulos, J. Appl. Phys. 117 (2015) 094305.
[14] P. Vogt, et al., Phys. Rev. Lett. 108 (2012) 155501.
[15] F. Zhai, K. Chang, Phys. Rev. B 77 (2008) 113409.
[16] E. Romera, J.B. Roldn, F. de los Santos, Phys. Lett. A 378 (2014) 2582.
[17] N. Singh, U. Schwingenschlgl, Phys. Status Solidi RRL 8 (2014) 353.
[18] H. Wang, X. Chena, B. Zhou, W. Liao, G. Zhou, Phys. B 406 (2011) 4407.
[19] D. Wang, Z. Huang, Y. Zhang, G. Jin, Phys. Rev. B 93 (2016) 195425.
[20] T. Yokoyama, Phys. Rev. B 87 (2013) 241409R.
[21] X.J. Qiu, Y.F. Cheng, Z.Z. Cao, J.M. Lei, J. Phys. D. Appl. Phys. 48 (2015) 465105.
[22] R. Saxena, A. Saha, S. Rao, Phys. Rev. B 92 (2015) 245412.
[23] A.B. Chen, X.F. Wang, P. Vasilopoulos, M.X. Zhai, Y.S. Liu, Phys. Chem. Chem. Phys. 16 (2014) 5113.
[24] V. Derakhshan, S.A. Ketabi, A.G. Moghaddam, Superlattice. Microst. 100 (2016) 214.
[25] D. Wang, G. Jin, Phys. Lett. A 378 (2014) 2557.
[26] S. Rachel, M. Ezawa, Phys. Rev. B 89 (2014) 195303.
[27] P.P. Freitas, R. Ferreira, S. Cardoso, F. Cardoso, J. Phys. Condens. Matter 19 (2007) 165221.
[28] Q. Ru-Ge, W. Yang-Yang, L. Jin, Chin. Phys. B 24 (2015) 088105.
[29] S. Stuart, et al., Nat. Mater. 3 (2004) 862.
[30] C. Xu, G. Luo, Q. Liu, J. Zheng, Z. Zhang, S. Nagase, Z. Gao, J. Lu, Nanoscale 4 (2012) 3111.
[31] J. Kang, F. Wu, J. Li, Appl. Phys. Lett. 100 (2012) 233122.
[32] D. Zhang, M. Long, X. Zhang, C. Cao, H. Xu, M. Li, K. Chan, Chem. Phys. Lett. 616 (2014) 178.
[33] C.C. Liu, H. Jiang, Y.G. Yao, Phys. Rev. B 84 (2011) 195430.
[34] S. Datta, Electronic Transport in Mesoscopic Systems, Cambridge University Press, 1995.
[35] M.I. Katsnelson, K.S. Novoselov, A.K. Geim, Nat. Phys. 2 (2006) 620.